Proceedings of ASME Turbo Expo 2025
Turbomachinery Technical Conference and Exposition
GT2025
June 16-20, 2025, Memphis, Tennessee

GT2025-151389

SURFACE ROUGHNESS EFFECTS ON THE OPERABILITY AND PERFORMANCE OF A HYDROGEN JET BURNER

Robin Vivoli
Cardiff University
Cardiff, Wales, UK

Daniel Pugh
Cardiff University
Cardiff, Wales, UK

Burak Goktepe
Cardiff University
Cardiff, Wales, UK

Sally Hewlett
Cardiff University
Cardiff, Wales, UK

Anthony Giles
Cardiff University
Cardiff, Wales, UK

Richard Marsh
Cardiff University
Cardiff, Wales, UK

Steven Morris
Cardiff University
Cardiff, Wales, UK

Philip Bowen
Cardiff University
Cardiff, Wales, UK

ABSTRACT

Over the past decade, Additive Manufacturing (AM) has gained considerable traction in the gas turbine industry. Manufacturers now look to AM for the production of critical components central to the combustor architecture. However, AM struggles to achieve satisfactory surface finishes, with its increased surface roughness shown to impact axial velocities, heat release, NO_x emissions, and stability limits. Correlations between increased roughness and boundary layer flashback resistance are of significant interest for lean premixed combustion of high hydrogen content (HHC) fuels. With the development of innovative burner configurations designed to address static stability issues in HHC fuels, and the growing use of AM in their fabrication, studying roughness effects on these designs is essential. This study aims to quantify the impact of surface roughness on an industry-relevant jet burner configuration, building on previous research by the authors using premixed swirl geometries. A premixed jet burner was developed with an interchangeable section to accommodate varying surface textures. The burner was characterized under atmospheric hydrogen-fired conditions at thermal powers ranging from 10 to 25 kW. Both smooth and rough inserts representing traditional machining and selective laser melting manufacturing techniques were utilized. The findings highlight how surface roughness influences flame topology, static stability, and emissions, providing an experimental basis for future numerical studies on roughness sensitivity in advanced burner designs.

Keywords: *Additive Manufacturing, Surface Roughness, Boundary Layer Flashback, Hydrogen Combustion.*

NOMENCLATURE

AM	Additive Manufacturing
BLF	Boundary Layer Flashback
CFD	Computational fluid dynamics
EDM	Electron discharge machining
GTRC	Gas Turbine Research Centre
HHC	High Hydrogen Content
LBO	Lean Blow-Off
LDA	Laser Doppler Anemometry
M1	Machined insert
PJB	Premixed Jet Burner
r	Radial coordinate
R2	Rough insert
Ra	Arithmetic Average Roughness
Re	Reynolds Number
Rq	RMS Surface Roughness
Rz	Ten-Point Average Roughness
SLM	Selective Laser Melting
TI	Turbulence Intensity
TP	Thermal Power
$\bar{u}$	Mean Nozzle Exit Axial Velocity
u	Axial Velocity
u'_{RMS}	Fluctuating Axial Velocity
u_{max}	Maximum Axial Velocity at Nozzle Exit
X_x	Mole Fraction of x
Φ	Equivalence Ratio

1. INTRODUCTION

Additive Manufacturing (AM) has seen increased utilization over the past decade thanks to its well-documented benefits [1–3]. Consequently, in the gas turbine industry, AM is being employed to produce and extend the life of critical components [4–6]. However, poor surface finish remains a major limitation

[7] with extra post-processing steps often required to reach an acceptable surface finish [8].

In gas turbine applications, experimental studies have demonstrated the influence of increased roughness of “raw” AM components on axial velocities, heat release, NO_x emissions, and operability limits in swirl-stabilized burners using both hydrocarbon and high hydrogen content (HHC) fuels [9,10]. Increased surface roughness has also been shown to enhance boundary layer flashback (BLF) resistance [11,12]. BLF occurs when the flame propagates upstream along the boundary layer of the flow, disrupting the premixing process and potentially causing damage or instability in the combustion system [13,14]. This phenomenon is especially critical for lean premixed combustion of HHC fuels, where the high diffusivity and reactivity of hydrogen significantly amplify the propensity for flashback [15–17]. Demonstrating that the inherent surface roughness of “raw” unprocessed AM components can improve BLF resistance would therefore indicate significant potential for commercial benefit. While Computational Fluid Dynamics (CFD) can offer deeper insights into these roughness effects by enabling detailed data analysis in areas that are difficult to access experimentally, accurately capturing these effects numerically has proven challenging [18–20]. Smooth and rough experimental benchmark data is essential for determining the appropriate parameter settings needed to accurately model roughness effects in state-of-the-art burner configurations.

Numerous innovative burner configurations are being developed to address the challenges posed by HHC fuels, with efforts focused on achieving safe and reliable hydrogen firing capabilities of up to 100 vol.-% [21–23]. One such burner architecture involves utilizing burners with a jet in crossflow configuration [22,23]. Such burners ensure rapid mixing and high bulk flow velocities which help reduce NO_x formation by minimizing residence time. The absence of flammable fuel/air mixtures prior to fuel injection prevents flashback from propagating further upstream thereby reducing the risk of significant damage.

As AM becomes increasingly integral to the production of novel burners and, given that surface roughness has known measurable effects on the performance of traditional burners, it is crucial to quantify the impact of roughness on this new generation of advanced combustion systems.

1.1. Research Scope

In the current study, the influence of surface roughness on an industry relevant jet burner configuration is quantified under hydrogen fired conditions at atmospheric pressure. Emissions and flame composition investigations are undertaken for thermal powers of 15, 20 and 25 kW over a range of equivalence ratios (Φ) (17976 – 71386 Reynolds Number), with a more detailed look at flashback limits performed at lower thermal powers (10, 12.5 and 15 kW) over a range of bulk exit velocities (14.2 – 18.75 m/s). A premixed jet burner has been designed with an interchangeable section near the end of the premixing chamber allowing studies of different surface textures. Initial characterization of the burner with a traditionally machined insert is performed prior to analyzing a rough insert. The latter represents a high surface roughness, serving as the worst-case surface finish achievable from a "raw" unprocessed AM component produced using Selective Laser Melting (SLM) [24]. This study aims to evaluate the effect of two surface roughness on flame shape, burner stability limits and emissions via high-speed, time-resolved velocimetry and OH* chemiluminescence.

The results of this study will also provide a detailed experimental basis for surface roughness analysis when dealing with state-of-the-art jet burner configurations. This includes providing a reference dataset for future numerical work where roughness sensitivity is to be performed.

2. EXPERIMENTAL AND DIAGNOSTIC SETUP

2.1. Premixed Jet Burner

All experimental work was conducted on a newly designed premixed jet burner inspired by industrial combustor architectures, as described by Krebs et al. [23]. In the reference burner, the high-velocity crossflow injection of fuel via a central fuel lance into the airstream promotes effective premixing. The potential for fuel/air unmixedness is removed by using a premixed charge, simplifying the rig both physically and numerically and ensuring that any changes observed when altering the surface finish can be attributed solely to the surface modification. Though fuel would no longer be injected radially into the air stream via a central fuel lance, a bluff body with the same outer dimensions is used to generate comparable velocity flow-fields downstream. Critical dimensions such as the premixing length and nozzle diameter were selected for industry relevance. The resulting assembly for this premixed jet burner (PJB) is shown in Fig. 1.

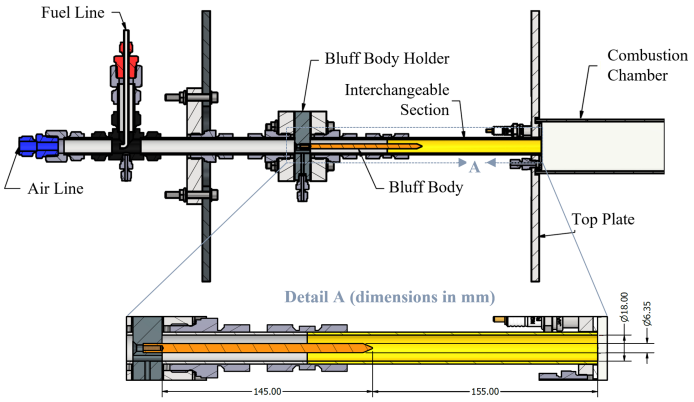

FIGURE 1: CROSS-SECTION VIEW OF THE PJB ASSEMBLY WITH DETAILED VIEW A HIGHLIGHTING CRITICAL DIMENSIONS.

The same underlying fuel and air delivery systems developed at Cardiff University’s Gas Turbine Research Centre (GTRC) for repeatable and fine control were employed as described in previous studies [20,25,26]. Dedicated flow control valves and Coriolis mass flowmeters were utilized on critical delivery lines. A variable speed drive air compressor paired with an air dryer ensured optimal air delivery. The 100% H_2 fuel flow,

delivered from multi-cylinder packs (N5 CP grade 99.999%) stored in a remote onsite location, is injected upstream of the bluff body assembly in a counterflow configuration to allow for a high level of premixing. A square cross-section quartz tube was used to confine the combustion chamber enabling optical access. The last part of the premixing section, shown in yellow in Fig. 1, was designed to be easily interchangeable and will serve as the area to analyze the effects of inserts with different finishes.

Holes were drilled into the top plate to allow for the insertion of the ignitor and instrumentation probes at the base of the combustion chamber as illustrated in Fig. 2. The ignitor was bent at a 90° angle from its insertion point to ensure it sparked against the tip of the burner outlet nozzle, minimizing its impact on the flow field. Thermocouples were positioned at the base of the combustion chamber and along the outer edge of the burner nozzle, mainly for monitoring conditions approaching flashback, lean flame blow-off (LBO) and to establish boundary conditions for future CFD simulations.

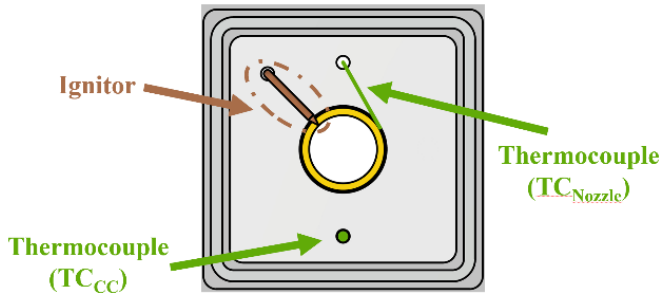

FIGURE 2: RADIAL VIEW OF INSTRUMENTATION AND IGNITOR LOCATION IN BURNER FACE OF THE PJB.

2.2. Interchangeable Insert Design and Manufacture

For this work, a comparison between surface textures produced by conventional manufacturing techniques and AM was undertaken. As previously mentioned, two interchangeable inserts were created: one was conventionally manufactured ("M1" in Fig. 3) with AM initially considered to produce the rough insert. However, due to the well-documented issues with warping [27,28], high costs, and difficulty in precisely controlling the surface finish [24], a more reliable method was chosen to replicate surface textures comparable to those achievable via AM.

Methods such as grit blasting and coating application were considered impractical for adding roughness to the inner walls of a long hollow cylinder. Drawing on the findings of Ablyaz et al. [29] and Karmiris-Obratański et al. [30], which demonstrated the suitability of Electron Discharge Machining (EDM) for creating a variety of surface textures on delicate and hard-to-reach parts, EDM was selected for texturing the rough insert ("R2" in Fig. 3). Both inserts were machined from round bar, the inner diameter of R2 being initially undersized to account for material loss during the EDM process, ensuring consistent final diameters. The two resulting inserts, along with example surface profiles that visually demonstrate changes in finish, are presented in Fig. 3.

Previous studies have shown that as-printed parts can be seen to present a wide range of surface finishes [24,31]. Psomoglou et al. [10] investigated roughness effects on AM swirlers with a maximum arithmetic average roughness (Ra) value of ≈ 9 µm. Since the roughness-induced changes observed were minimal, investigations at higher surface roughness were advised. For this work, an R2 insert with a surface finish of Ra ≈ 20 µm was therefore selected to represent AM downskin surfaces with an angled build orientation. This choice reflects the well-documented observations that a worsening surface finish is primarily influenced by the laser incidence angle deviating further from horizontal and the challenges associated with downward-facing surfaces during the printing process [32,33]. By adopting such an approach, the usefulness of not only surface polishing but also the addition of artificially increased roughness would be assessed.

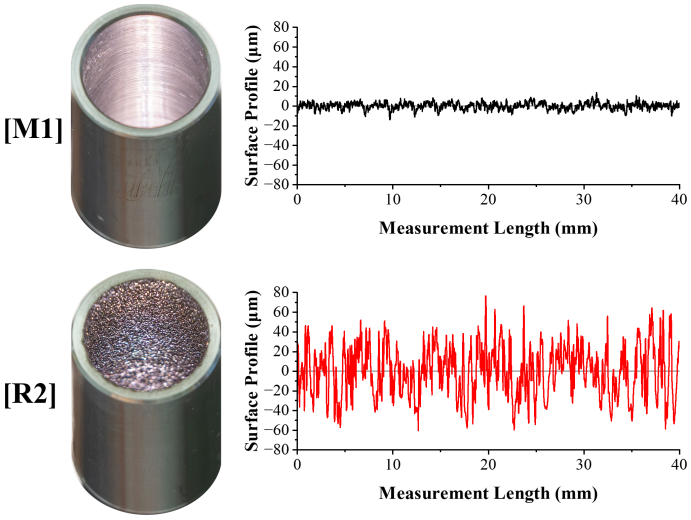

FIGURE 3: CONVENTIONALLY MACHINED (M1) AND EDM (R2) INTERCHANGEABLE INSERTS WITH RESPECTIVE SURFACE PROFILES MEASURED VIA THE PROFILOMETER DESCRIBED IN SECTION 2.3.

2.3. Surface Roughness Measurements

The form and surface roughness of all interchangeable inserts were measured using a Taylor Hobson Form TalySurf Series 2 profilometer, used extensively for tribology and SLM surface roughness studies [9,34,35]. A standard inductive pick-up stylus arm equipped with a 90° conisphere diamond stylus, featuring a 2 µm nominal radius and a vertical resolution of 16 nm, was employed. Measurements and surface roughness analysis were conducted in accordance with BS EN ISO 4287/4288 guidelines, as far as reasonably practical. Given that the rough insert was expected to have an average surface roughness of 20 µm, an 8 mm cut-off length was used. For the machined insert, a cut-off length of 0.8 mm was applied.

Roughness measurements were taken at both ends of each insert, with all measurements spanning a 40 mm evaluation length. After each reading, the insert was rotated by 120° to take the next measurement. As shown in Fig. 4, this process resulted in six measurements per insert, providing a detailed profile of internal surface roughness, capturing any variations in surface finish along each cylinder.

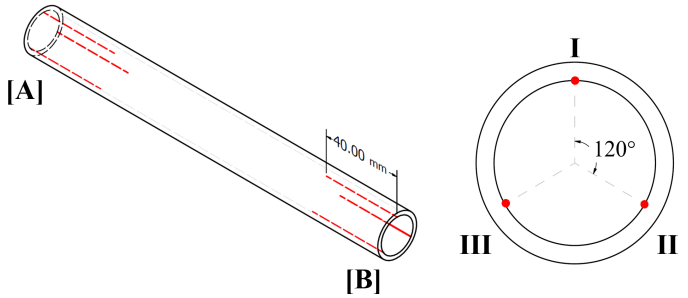

FIGURE 4: SURFACE ROUGHNESS MEASUREMENT LOCATIONS ON M1 AND R2 INSERTS.

2.4. Emissions Measurements

Exhaust gas sampling and analysis were carried out using a standard industry system supplied by Signal Gas Analysers Ltd. A single point probe was positioned 170 mm downstream along the centerline of the burner, remaining within the quartz confinement to prevent atmospheric entrainment. The 50 m sample line was maintained at a temperature of 453 K. To minimize losses, NO measurements were performed hot and wet using a heated vacuum chemiluminescence analyzer (Signal Instruments 4000VM). Additional flow was passed through a chiller to reduce molar water concentration below 1% before exhaust molar O_2 measurements were made using a paramagnetic analyzer (Signal Instruments 9000MGA).

NO_x emissions were normalized to a reference value of dry, 15% O_2 concentration via equations 1 and 2 respectively. Although it is recognized that this emission reporting method can overstate pollutant concentrations for HHC fuels when comparing with hydrocarbons [36], the dry 15% O_2 method was considered appropriate since this study does not focus on fuel switching.

$$NO_{dry} = \frac{NO_{measured}}{1 - \chi_{H_2O}} \quad (1)$$

Exhaust water fractions (χ_{H_2O}) were obtained from equilibrium modeling. Measured dry O_2 fractions (χ_{O_2}) were then used to subsequently normalize readings to an equivalent reference 15% O_2 as shown in the following equation, in accordance with ISO 11042 [37]:

$$NO_{dry\,15\%\,O_2} = NO_{dry} \cdot \left(\frac{0.209 - 0.15}{0.209 - \chi_{O_2}}\right) \quad (2)$$

Typical uncertainties of approximately ±5% of measurement account for analyzer specifications, linearization, and accuracy in span gas certification.

2.5. Chemiluminescence

Roughness induced changes in the flame topology were characterized via the use of high-speed OH^* chemiluminescence imaging focusing on the well-known $A^2\Sigma^+ \rightarrow X^2\Pi$ OH* system [38]. Data collection was performed via a Phantom v1212 high-speed CMOS camera, a Specialized Imaging SIL40HG50 high-speed image intensifier, a UV lens (78mm F/4), and a 315 nm (±15 nm FWHM) narrow bandpass filter. Further information on this high-speed imaging setup can be found in other works [9,39].

Chemiluminescence data was recorded at 4 kHz, with the image intensifier gated at 10 µs. A scaled target image was used to determine the image resolution, which was equal to 4 pixels/mm. The camera resolution was scaled down to reduce file sizes to 400 x 800 pixels, resulting in a field of view of 200 mm (axial, y) by 100 mm (radial, x). Each chemiluminescence dataset was time-averaged over 2000 images (duration of 0.5 s). Post-processing was then performed using a modified Abel inversion algorithm to produce a planar representation of the three-dimensional flame brush, as described in previous studies [39,40]. Due to space constraints, only Abel-deconvoluted half-flames are presented in this paper, while the raw dataset is available in the institutional repository.

2.6. High-Speed Velocimetry

A 1D Dantec Dynamics Flowlite Laser Doppler Anemometry (LDA) System, described in detail in previous studies [9], was used for characterizing the mean flow field and turbulence characteristics of isothermal airflow exiting the burner nozzle. Three isothermal air flow conditions were investigated, with equivalent total mass flow of $\Phi = 0.4$ at 25kW ($\bar{u} = 66.2$ m/s), $\Phi = 0.7$ at 20kW ($\bar{u} = 33.6$ m/s) and $\Phi = 0.93$ at 15kW ($\bar{u} = 20.5$ m/s). This allows roughness effects to be assessed across mean bulk nozzle exit axial velocities ($\bar{u}$) ranging from 20 m/s to 60 m/s. The airflow was seeded with Al_2O_3 particles of nominal 1 µm diameter. The burst signal was processed using a BSA F60 processor and Dantec BSA Flow Software to determine the mean and RMS velocities at the control volume. In this study both mean (u) and fluctuating (u'_{RMS}) axial velocities were measured 2 mm downstream of the burner exit nozzle. The transmitter and receiver optics were mounted on a traverse system, allowing the control volume to be positioned across the flow field. Measurements were taken starting and ending 1.5 mm outside the nozzle exit at 0.5 mm increments for the outermost 2.5 mm of radial travel. Beyond this, measurements were taken at 1 mm intervals across the remaining range (-8 mm ≤ r ≤ 8 mm), resulting in a total of 27 data points. To investigate the near-wall velocity and turbulence intensity at the burner exit, the isothermal flow measurements were conducted with the quartz confinement removed. By controlling the seeding rate and density, data capture rates of up to 3500 points or 10 seconds of acquisition time were achieved.

TABLE 1: SURFACE ROUGHNESS MEASUREMENTS FOR EACH INSERT.

Insert	Measurement	Measurement Location						Average (µm)
		A			B			
		I	II	III	I	II	III	
M1	R_a (µm)	1.79	1.89	1.8	1.6	1.77	1.52	1.73
	R_z (µm)	9.54	9.96	9.58	9.08	9.39	8.43	9.33
	R_q (µm)	2.19	2.3	2.19	2.01	2.17	1.89	2.13
R2	R_a (µm)	21.4	21.9	26.3	19.4	19.9	18.3	21.20
	R_z (µm)	139	137	146	118	138	116	132.33
	R_q (µm)	26.9	27.2	32.2	23.5	25.6	22.5	26.32

3. RESULTS AND DISCUSSION

3.1. Surface Finish and Form Deviation

Prior to conducting any experimental work, the surface finish and inner diameters of each insert were assessed. Average Ra, Rq (RMS surface roughness), and Rz (ten-point average roughness) values for each insert are presented in Table 1. Additional details on the surface roughness quantifications mentioned above can be found in standards such as BS 1134:2010 [41]. A comparison of the average surface finishes achieved for both the M1 and R2 inserts reveals an order of magnitude difference. The R2 insert closely aligns with the target roughness of ~20 µm Ra. For the M1 insert, surface roughness measurements remain consistent both radially and axially. Higher inconsistencies are observed for the R2 insert primarily due to electrode wear during the manufacturing process. Overall, the increased surface finish variation of R2 compared to M1 would also be expected in AM processes, as it is well-documented that surface roughness along the length of AM components varies discontinuously without a clear trend [42].

Form deviation of the R2 insert relative to the smooth reference was assessed by fitting a curve to radial TalySurf measurements via the TalyMap Platinum 7.1.7288 software. Measurements showed radii to be within ±0.100 mm of the reference, with deviations similar to those of other AM components found in the literature [43,44]. Area differences between the two inserts were found to be ~1.78%.

3.2. Flow Characterization

Understanding the effects of increased surface roughness on the flow-field is of crucial importance for gaining deeper insights into the phenomena discussed in the following sections. LDA is an effective tool for this purpose, as it offers simultaneous temporal and spatial measurements of both mean and fluctuating axial velocity components. By combining u and u'_{RMS}, turbulence intensity (TI) can be quantified as shown in Equation 3:

$$TI\ (\%) = \left(\frac{u'_{RMS}}{u}\right) * 100 \qquad (3)$$

Axial velocity and TI profiles taken 2 mm downstream of the nozzle exit are shown in Fig. 5 and 6. It is important to note that, in the area outside the nozzle inner diameter (r < -10 mm or r > 10 mm), while measurements were taken, particle detection rates were often too low to produce usable data. As a result, both axial velocity and turbulence data were truncated at the boundary of this range. Three isothermal air flow conditions were investigated, with equivalent total mass flow to Φ = 0.4 at 25kW, Φ = 0.7 at 20kW and Φ = 0.93 at 15kW combustion conditions. The latter flow rate was chosen because, under equivalent combustion conditions, flashback occurred with the M1 insert only as discussed in Section 3.3.2. The other two flow rates were selected to examine potential changes in the effects of roughness at progressively higher Reynolds numbers (Re). Bulk flow and maximum axial velocities recorded at each isothermal condition together with percentage differences between M1 and R2 flows, and respective Re are collated in Table 2.

TABLE 2: BULK AND MAXIMUM AXIAL VELOCITIES AT THE NOZZLE EXIT FOR ALL ISOTHERMAL CASES, ALONG WITH THE PERCENTAGE VARIATIONS BETWEEN M1 AND R2 VALUES AND THE CORRESPONDING RE.

		Φ = 0.93 at 15kW	Φ = 0.7 at 20kW	Φ = 0.4 at 25kW
$\bar{u}$ (m/s)	theoretical	20.5	33.6	66.2
	M1	19.4	32.1	62.9
	R2	19.6	32.09	65.1
	%	1.1	-0.06	3.51
u_{max} (m/s)	M1	22.5	36.6	70.7
	R2	23.3	38.2	75.3
	%	3.9	4.3	6.5
Re		24169	39825	79387

Table 2 demonstrates a strong correlation between the theoretical bulk flow velocities, calculated from first principles, and the experimentally measured values. Differences in peak axial velocities were observed between the M1 and R2 inserts, with the R2 cases consistently exhibiting higher velocities. This increase in relative velocity with increasing roughness is proportional to the overall bulk flow velocity. Since the overall bulk flows remain largely unchanged between the respective M1 and R2 cases, this suggests a shift in the overall velocity profiles.

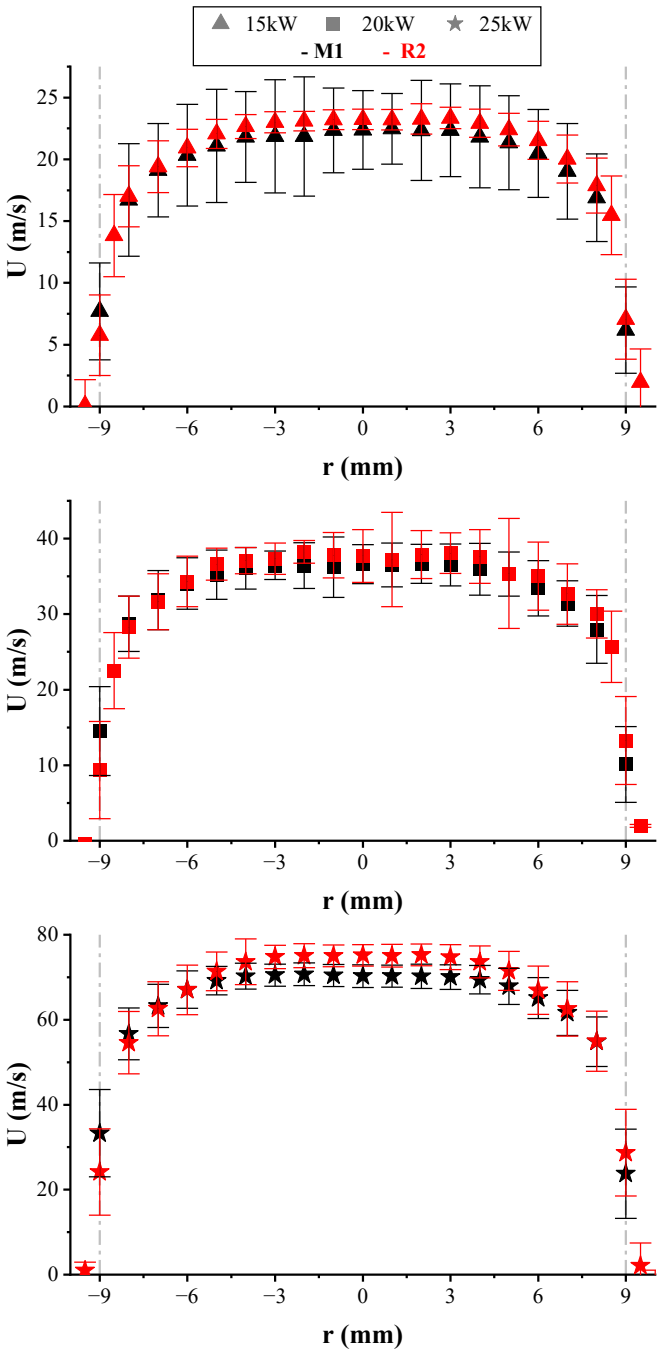

FIGURE 5: AXIAL VELOCITY PROFILES AT EQUIVALENT AIR FLOW TO 15 KW AT Φ = 0.93, 20 KW AT Φ = 0.7 AND 25 KW AT Φ = 0.4. NOTE THE CHANGE IN Y AXIS SCALE. VERTICAL LINES AT ± 9 MM SHOWING ID OF BURNER NOZZLE.

From Fig. 5, all M1 velocity profiles exhibit a flatter and broader profile than the respective R2 counterparts. The latter presenting lower velocities in the boundary layer likely due to an increase in the turbulence intensity near the wall. The relatively higher axial velocities observed in the core flow for the R2 cases can be attributed to a virtual reduction in the effective diameter of the pipe, resulting from the accelerated boundary layer growth caused by the rough elements [45], the effect being amplified as the Reynolds Number increases. Regarding the error bars, calculated using u'_{RMS} values collected at each point, it is evident that as velocities increase, the overall error decreases.

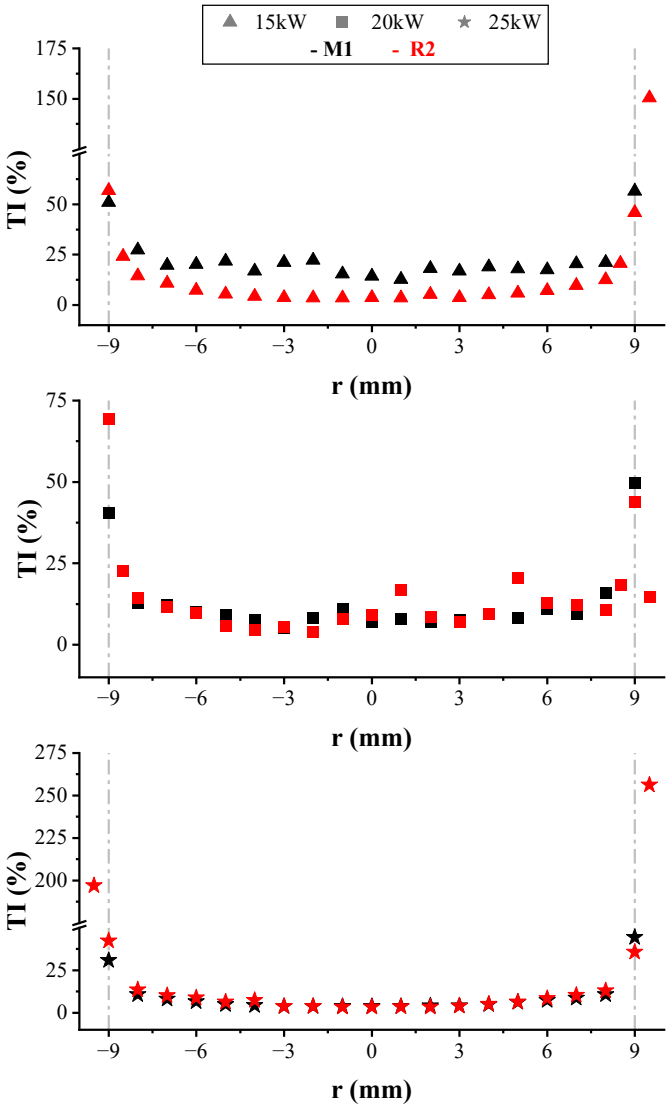

FIGURE 6: TURBULENCE INTENSITY PROFILES AT EQUIVALENT AIR FLOWS TO 15 KW AT Φ = 0.93, 20 KW AT Φ = 0.7 AND 25 KW AT Φ = 0.4. NOTE BREAKS IN THE Y-AXIS FOR TOP AND BOTTOM PLOTS. VERTICAL LINES AT ± 9 MM SHOWING ID OF BURNER NOZZLE.

Figure 6 indicates that, for the 15 kW flow conditions (without fuel flow and hence isothermal), the M1 flow field presents greater turbulence in the core flow compared to its R2 counterpart, while the latter shows higher turbulence in the boundary layer region (± 9 mm). Similarly, in the 25 kW isothermal case, the R2 insert also demonstrates increased turbulence in the boundary layer. For the 20 kW and 25 kW isothermal conditions, differences in turbulence within the core

flow (-4 mm ≤ r ≤ 4 mm) are less pronounced, with average R2 values being approximately 2.9% and 4.5% higher than M1 values for the 20 kW and 25 kW isothermal cases, respectively. This suggests that, particularly at higher flowrates, surface roughness has a greater effect on boundary layer turbulence compared to that in the core flow. These variations, also reflected in the velocity profile changes shown in Fig. 5, help explain the differences in operability limits between the M1 and R2 inserts discussed in Section 3.3.2.

3.3. Flame Behavior and Stability

3.3.1. Flame location

Combustion experiments were performed under thermal powers ranging from 10 to 25 kW with detailed OH* chemiluminescence data collected for 15 kW, 20 kW and 25 kW conditions. A full operability sweep from LBO to flashback was performed by varying Φ for all three thermal powers utilizing both inserts. If flashback conditions were not encountered, the operability sweep was terminated upon reaching stoichiometry (Φ = 1). At each thermal power, OH* chemiluminescence data was collected at 0.1 increments between 0.4 ≤ Φ ≤ 1. For the M1 insert, the Φ = 1.0 case was not recorded at 15 kW as flashback occurred prior to reaching stoichiometry. Although the flame began showing signs of lift-off at Φ = 0.4 across all thermal power levels, the data was presented to emphasize any roughness-induced changes as the system approached LBO. Abel-transformed OH* chemiluminescence images for all three thermal powers are shown in Fig. 7 and 8. Each image represents a combination of both the M1 (left half) and R2 (right half) half-flame for the given thermal power and Φ, where the left and right flames in each image correspond to M1 and R2 inserts respectively. As a result, the field of view expands axially downstream from burner exit nozzle (y = 0 mm) and radially outward from the inner edge of the quartz confinement (M1 = 0 mm ≤ r ≤ 32 mm, R2 = 32 mm < r ≤ 64 mm). Images for each Φ are shown with colormaps normalized to the maximum OH* intensity in each half-flame. To avoid any issues with flame asymmetry the right-hand half-image is shown for both M1 and R2 flames, the M1 half-flame being mirrored horizontally prior to aligning it with the respective R2 half-flame.

In Fig. 7 and 8 it is observed that the flame moves upstream toward the burner exit with increasing Φ, irrespective of the insert. This behavior occurs due to a combination of decreased axial velocity and higher flame speed. In addition, for a given Φ, the flame length increases with thermal power primarily due to the increase in bulk flow velocity. At Φ = 0.4, the flame becomes progressively lifted with increasing thermal power. Focusing on the 25 kW case at Φ = 0.4, the R2 flame appears noticeably more lifted than the M1 counterpart, suggesting that increased surface roughness leads to an earlier onset of flame lift-off and, subsequently, LBO. A detailed analysis of the effects of roughness on stability limits is provided in Section 3.3.2.

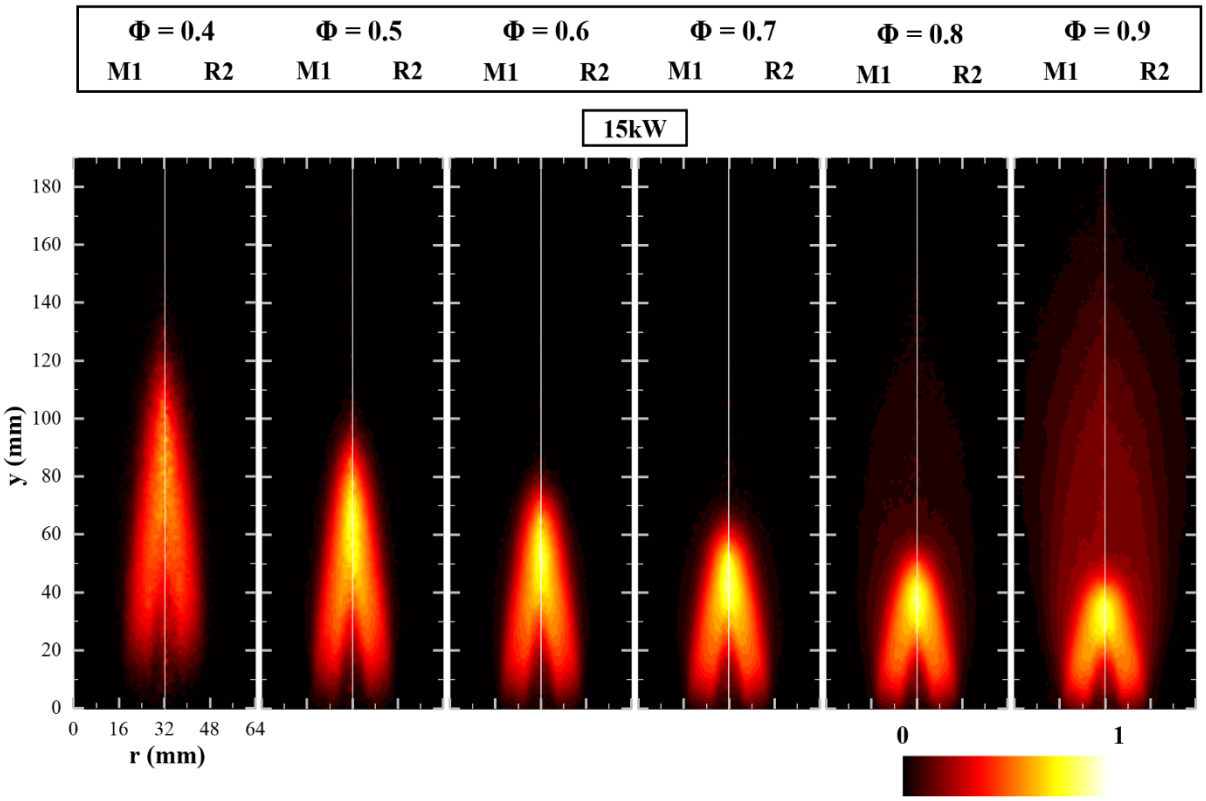

FIGURE 7: ABEL TRANSFORMED OH* CHEMILUMINESCENCE IMAGES FOR 15 KW OVER A RANGE OF Φ. COLORMAP NORMALIZED TO MAXIMUM OH* INTENSITY IN EACH HALF IMAGE. M1 RESULTS SHOWN ON THE LEFT AND R2 RESULTS SHOWN ON THE RIGHT FOR EACH CONDITION.

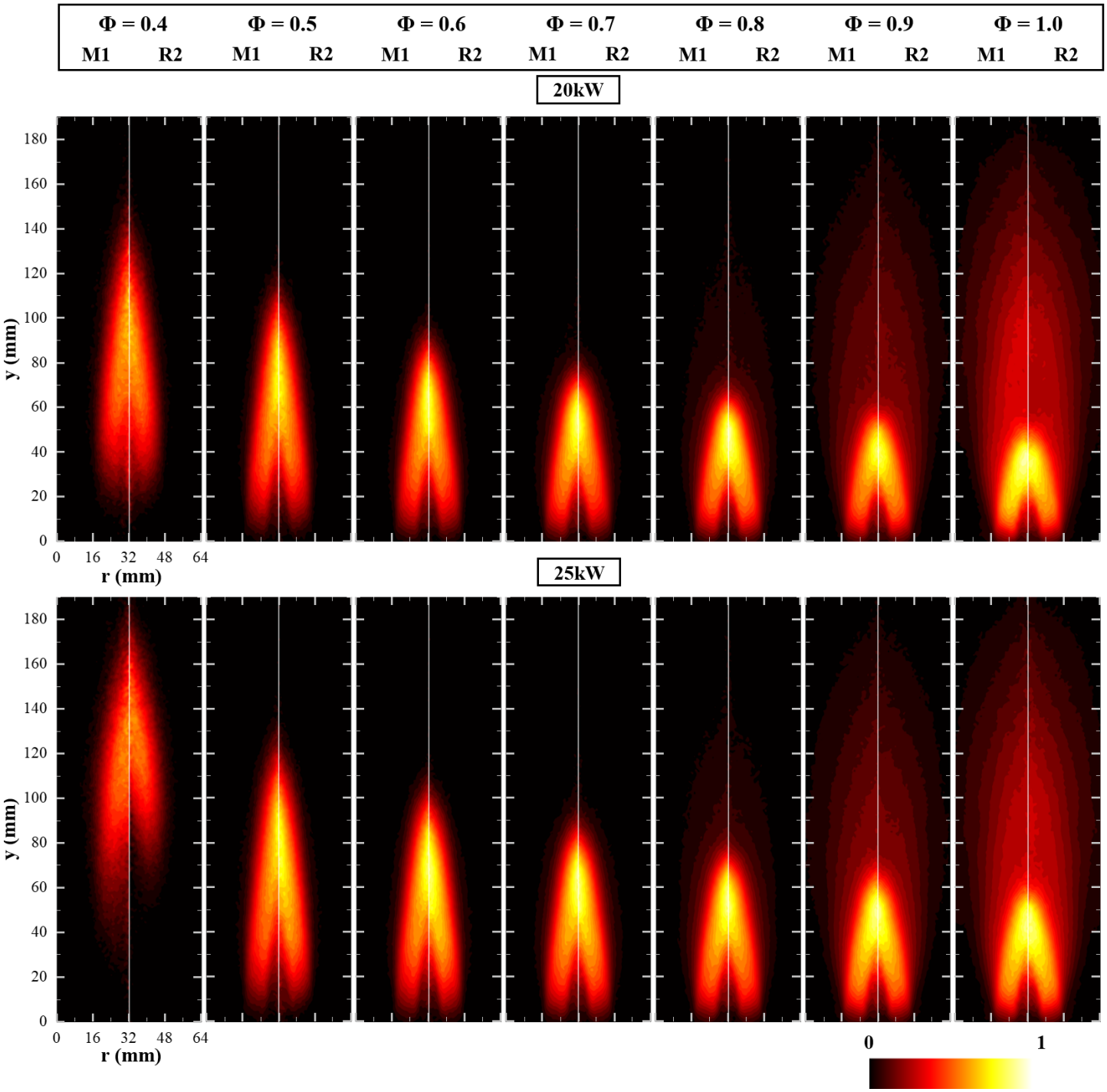

FIGURE 8: ABEL TRANSFORMED OH* CHEMILUMINESCENCE IMAGES FOR 20 KW [TOP] AND 25 KW [BOTTOM] THERMAL POWERS OVER A RANGE OF Φ. COLORMAP NORMALIZED TO MAXIMUM OH* INTENSITY IN EACH HALF IMAGE. M1 RESULTS SHOWN ON THE LEFT AND R2 RESULTS SHOWN ON THE RIGHT FOR EACH CONDITION.

Variations in the peak OH* intensity were found to neither be significant nor exhibit a consistent trend, indicating that surface roughness did not impact heat release intensity. However, changes in the overall flame shape were noted. For the same equivalence ratio and thermal power, the R2 flame is observed to shift axially upstream while remaining largely unchanged radially. This axial shortening becomes more pronounced as the equivalence ratio is reduced and thermal power increased. To better visualize shifts in the flame and heat release center positions, the OH* chemiluminescence intensity centroid was calculated for both the raw averaged and Abel-deconvoluted half-flames across all cases, following the

procedure described in [26]. Consistent trends were observed for both the raw average and Abel-deconvoluted centroid locations. Therefore, for brevity, only the raw average coordinates will be presented as shown in Fig. 9.

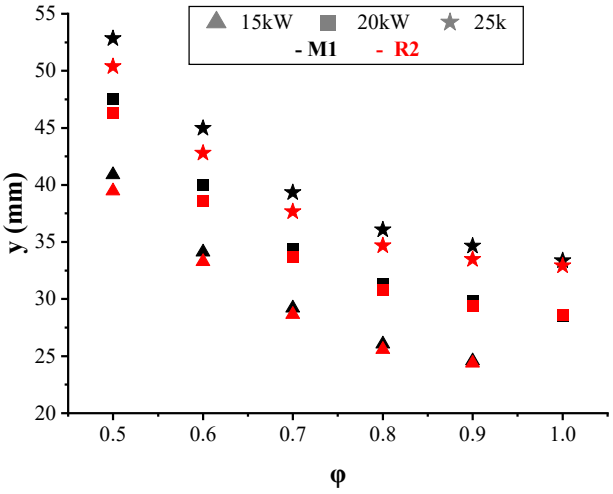

FIGURE 9: AXIAL RAW AVERAGED OH* CENTROID LOCATION MOVEMENT.

Radial shifts in centroid location were found to be small and lack a consistent trend when compared with the axial shifts. The average radial deviation of the R2 flame compared with the M1 flame was in fact only found to be ~ 1.4%. To simplify the presentation of the data, only the axial coordinates for both M1 and R2 inserts are plotted in Fig. 9 for all thermal powers and $0.5 \leq \Phi \leq 1$. The $\Phi = 0.4$ centroid locations were excluded, as the flame was lifted and unstable at this equivalence ratio, particularly at higher thermal powers, preventing reliable representation of centroid location changes.

From Fig. 9, the magnitude of axial shortening in the R2 flames increases with both higher thermal power and lower equivalence ratios, suggesting that susceptibility is proportional to the bulk flow velocity. At the $\Phi = 0.5$ conditions in fact, the percentage shortening of the R2 flame compared to the M1 flame increases by ~33% and ~83% for the 20 kW and 25 kW cases respectively compared to the corresponding 15 kW shortening. This axial shortening is likely driven by roughness-induced turbulence, particularly within the boundary layer, as demonstrated in Section 3.2, which enhances mixing and increases local burning rates. The effect becomes more pronounced at higher bulk flows and lower equivalence ratios, where the flame is more sensitive to turbulence-induced enhancements.

3.3.2. Stability Limits

Operability sweeps were conducted for 15 kW, 20 kW, and 25 kW, as described in Section 3.3.1. However, flashback was observed only at 15 kW and exclusively with the M1 insert. Recognizing the significant influence of surface finish on flashback behavior, a more detailed investigation was carried out at lower thermal powers. For this study, thermal powers of 10 kW, 12.5 kW, and 15 kW were tested, with flashback occurring for both inserts at all power levels except 15 kW for the range of Φ investigated. Each flashback condition was repeated twice for every thermal power, allowing sufficient time between tests for the burner to thermally stabilize. Results are shown in Fig. 10.

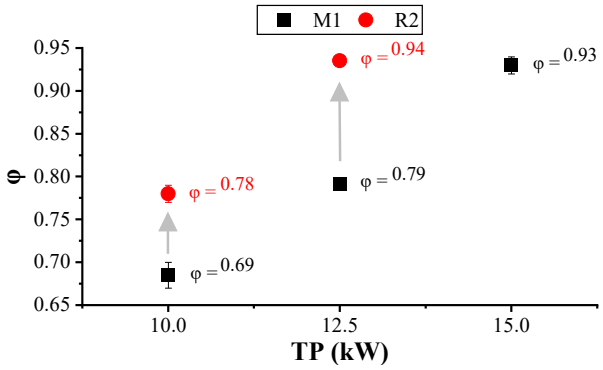

FIGURE 10: POWER SETTING VS. Φ AT THE POINT OF FLASHBACK TO DEMONSTRATE ROUGHNESS INDUCED CHANGES IN FLASHBACK BEHAVIOR.

Surface roughness was also found to influence LBO limits as mentioned in Section 3.3.1. Although LBO was not investigated for the lower thermal powers of 10 kW and 12.5 kW, at thermal powers between 15 kW and 25 kW, LBO was found to occur on average at ~2.5% higher equivalence ratios as shown in Fig. 11.

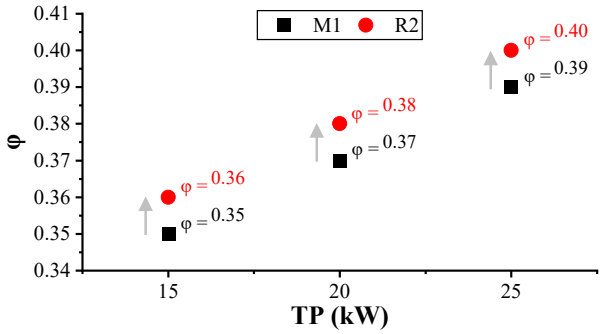

FIGURE 11: POWER SETTING VS. Φ AT THE POINT OF BLOWOFF TO DEMONSTRATE ROUGHNESS INDUCED CHANGES IN LBO BEHAVIOR.

The results in Fig. 10 demonstrate that surface roughness has a measurable impact on the burner flashback limits. At all thermal powers investigated the R2 insert exhibited greater flashback resistance compared to the M1 insert. For the same thermal power, the R2 cases flashed back at a higher Φ (lower relative $\bar{u}$) than with the M1 insert. In addition, the flashback resistance seems to increase with increasing thermal power. At 10 kW, flashback with the R2 insert occurred at ~13% higher Φ than with the M1 insert whilst at 12.5kW it occurred at ~19% higher Φ.

The observed shifts in both flashback and LBO to higher Φ can be partially attributed to the increased centerline velocities

at the nozzle exit, as identified isothermally in Section 3.2. Flashback exhibiting a more pronounced shift due to its greater sensitivity to local velocity variations and turbulence near the walls, whereas LBO is primarily governed by global turbulent flame speed. The significantly greater impact of roughness on flashback compared to LBO suggests that increased surface roughness positively influences operability limits.

3.4. Exhaust Gas Emissions

Exhaust NO_x emission measurements were taken at $\Phi = 0.5$, $\Phi = 0.6$ and $\Phi = 0.7$ for thermal powers between 15 kW and 25 kW as shown in Fig. 12. In these lean premixed flames, NO_x production is expected to be primarily driven by the thermal NO_x pathway [46]. However, since surface roughness has already been shown to influence flame position, stability limits, flow-fields and turbulence, measurable changes in NO_x may be observed.

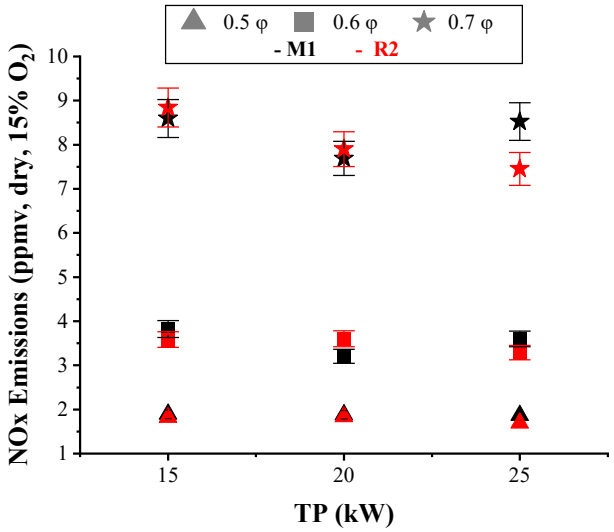

FIGURE 12: NO_X EMISSIONS AS A FUNCTION OF THERMAL POWER AND SURFACE ROUGHNESS.

From Fig. 12, it can be observed that NO_x emissions below 10 ppm were achieved across all test points investigated with values at $\Phi = 0.5$ and $\Phi = 0.6$ being below 5ppm. For these two equivalence ratios, the minor differences observed between the M1 and R2 cases did not allow for significant conclusions. Similar findings were noted for the lower two thermal powers, where measured differences were within the error bars. A more significant effect was observed at $\Phi = 0.7$ for the 25kW case, where NO_x emissions decrease by ~12.6% as surface roughness increased.

4. CONCLUSIONS

The impact of surface roughness on the performance indicators of a recently designed, industry-relevant generic premixed jet burner fired on hydrogen was investigated under atmospheric operational conditions. Guided by recent developments, two interchangeable inserts were utilized: one conventionally machined, representing the smooth benchmark, the other having a rough surface, mimicking unprocessed "raw" AM components. Detailed experimental characterization was performed, including measurements of emissions, flame behavior, and stability limits. By isolating surface finish as the primary variable, building on previous research, the study offers valuable insights into the implications of roughness for burner operability and emissions.

Key findings of this work are as follows:

- Increased roughness was associated with significant changes in stability limits. The rough insert (R2) demonstrated a wider stable operating range with measurably improved flashback resistance at the cost of marginally higher sensitivity to flame lift-off and LBO.
- Surface roughness caused an impact in flame position, with the R2 insert showing a repeatable upstream shift of the flame centroid, especially at higher thermal powers and lower equivalence ratios. This was accompanied by increased turbulence in the boundary layer leading to measurable differences in axial velocity distributions.
- NO_x emissions were consistently low across the range of conditions considered, with slight reductions observed for the rough insert at higher thermal powers, suggesting that roughness may marginally improve emission profiles due to slight mixing improvements.

These results underscore the importance of considering surface roughness effects in the design of hydrogen combustion systems, particularly in contexts where AM is used. The study demonstrates that adopting post-processing AM components to achieve smoother surfaces may not only be unnecessary but could also diminish performance, suggesting the potential for commercial benefit. Furthermore, this comprehensive dataset provides a foundation for refining reacting computational models with roughness sensitivity on novel state-of-the-art burner geometries.

ACKNOWLEDGEMENTS

This work was supported by the Engineering and Physical Sciences Research Council (EPSRC), Cardiff School of Engineering and Siemens Energy Industrial Turbomachinery Ltd. through the Centre for Doctoral Training in Resilient Decarbonized Fuel Energy Systems [Grant Number EP/S022996/1]; and HYFLEPOWER. Jadeed Beita and Suresh Sadasivuni are acknowledged for their invaluable feedback and guidance throughout this work. Dr. Alastair Clarke is acknowledged for his support in the surface roughness measurements. Finally, Jack Thomas is acknowledged for his efforts in operating and maintaining the experimental facility.

REFERENCES

[1] Dutta B, Babu S, Jared BH. Science, technology and applications of metals in additive manufacturing. Elsevier; 2019.

[2] Srinivasan D, Ananth K. Recent Advances in Alloy Development for Metal Additive Manufacturing in Gas Turbine/Aerospace Applications: A Review. J Indian Inst Sci 2022;102:311–49. https://doi.org/10.1007/s41745-022-00290-4.

[3] Gebisa AW, Lemu HG. Additive Manufacturing for the Manufacture of Gas Turbine Engine Components: Literature Review and Future Perspectives. Volume 6: Ceramics; Controls, Diagnostics, and Instrumentation; Education; Manufacturing Materials and Metallurgy, American Society of Mechanical Engineers; 2018. https://doi.org/10.1115/GT2018-76686.

[4] Navrotsky V, Graichen A, Brodin H. Industrialisation of 3D printing (additive manufacturing) for gas turbine components repair and manufacturing. VGB PowerTech 2015;12:48–52.

[5] Durocher A, Fan L, Francolini B, Füri M, Bourque G, Sirois J, et al. Characterization of a Novel Additive Manufacturing Micromix Nozzle Burning Methane to Hydrogen. J Eng Gas Turbine Power 2024;146. https://doi.org/10.1115/1.4063690.

[6] Andersson O, Graichen A, Brodin H, Navrotsky V. Developing Additive Manufacturing Technology for Burner Repair. J Eng Gas Turbine Power 2017;139. https://doi.org/10.1115/1.4034235.

[7] Calignano F, Manfredi D, Ambrosio EP, Iuliano L, Fino P. Influence of process parameters on surface roughness of aluminum parts produced by DMLS. The International Journal of Advanced Manufacturing Technology 2013;67:2743–51. https://doi.org/10.1007/s00170-012-4688-9.

[8] Shinonaga T, Kobayashi H, Okada A, Tsuji T. Surface smoothing of additively manufactured Ti-6Al-4V alloy by combination of grit blasting and large-area electron beam irradiation. The International Journal of Advanced Manufacturing Technology 2023;127:5127–37. https://doi.org/10.1007/s00170-023-11857-5.

[9] Runyon J, Giles A, Marsh R, Pugh D, Goktepe B, Bowen P, et al. Characterization of Additive Layer Manufacturing Swirl Burner Surface Roughness and Its Effects on Flame Stability Using High-Speed Diagnostics. J Eng Gas Turbine Power 2020;142. https://doi.org/10.1115/1.4044950.

[10] Psomoglou I, Goktepe B, Crayford A, Bowen P, Morris S, Jones N. Influence of AM Generated Burner Surface Roughness on NO_x Emissions and Operability of Hydrogen-Rich Fuels. Combustion Science and Technology 2024:1–20. https://doi.org/10.1080/00102202.2024.2390699.

[11] Ding S, Huang K, Han Y, Valiev D. Numerical study of the influence of wall roughness on laminar boundary layer flashback. Phys Rev Fluids 2021;6:023201. https://doi.org/10.1103/PhysRevFluids.6.023201.

[12] Al-Fahham M, Hatem FA, Alsaegh AS, Valera Medina A, Bigot S, Marsh R. Experimental Study to Enhance Resistance for Boundary Layer Flashback in Swirl Burners Using Microsurfaces. Volume 4A: Combustion, Fuels and Emissions, American Society of Mechanical Engineers; 2017. https://doi.org/10.1115/GT2017-63367.

[13] Boyce MP. Advanced industrial gas turbines for power generation. Combined Cycle Systems for Near-Zero Emission Power Generation, Elsevier; 2012, p. 44–102. https://doi.org/10.1533/9780857096180.44.

[14] du Toit MH, Avdeenkov A V., Bessarabov D. Reviewing H2 Combustion: A Case Study for Non-Fuel-Cell Power Systems and Safety in Passive Autocatalytic Recombiners. Energy & Fuels 2018;32:6401–22. https://doi.org/10.1021/acs.energyfuels.8b00724.

[15] Ebi D, Bombach R, Jansohn P. Swirl flame boundary layer flashback at elevated pressure: Modes of propagation and effect of hydrogen addition. Proceedings of the Combustion Institute 2021;38:6345–53. https://doi.org/10.1016/j.proci.2020.06.305.

[16] Reichel TG, Terhaar S, Paschereit O. Increasing Flashback Resistance in Lean Premixed Swirl-Stabilized Hydrogen Combustion by Axial Air Injection. J Eng Gas Turbine Power 2015;137. https://doi.org/10.1115/1.4029119.

[17] Kıymaz TB, Böncü E, Güleryüz D, Karaca M, Yılmaz B, Allouis C, et al. Numerical investigations on flashback dynamics of premixed methane-hydrogen-air laminar flames. Int J Hydrogen Energy 2022;47:25022–33. https://doi.org/10.1016/j.ijhydene.2022.05.230.

[18] Bons JP. A review of surface roughness effects in gas turbines. J Turbomach 2010;132. https://doi.org/10.1115/1.3066315.

[19] Stripf M, Schulz A, Bauer H-J. Modeling of Rough-Wall Boundary Layer Transition and Heat Transfer on Turbine Airfoils. J Turbomach 2008;130. https://doi.org/10.1115/1.2750675.

[20] Psomoglou I. Influence of surface roughness on burner characteristics and combustion performance of AM combustors. Doctor of Philosophy. Cardiff University, 2023.

[21] Vandervort C, Leach D, Walker D, Sasser J. Commercialization and Fleet Experience of the 7/9HA Gas Turbine Combined Cycle. ASME Turbo Expo 2019: Turbomachinery Technical Conference and Exposition, Phoenix, Arizona, USA: 2019.

[22] Funke HH-W, Beckmann N, Abanteriba S. An overview on dry low NOx micromix combustor development for hydrogen-rich gas turbine applications. Int J Hydrogen Energy 2019;44:6978–90. https://doi.org/10.1016/j.ijhydene.2019.01.161.

[23] Krebs W, Schulz A, Witzel B, Johnson C, Laster W, Pent J, et al. Advanced Combustion System for High Efficiency (ACE) of the new SGT5/6-9000HL Gas Turbine. Proceedings of ASME Turbo Expo 2022, Rotterdam: 2022, p. 1–11.

[24] Majeed A, Ahmed A, Salam A, Sheikh MZ. Surface quality improvement by parameters analysis,

optimization and heat treatment of AlSi10Mg parts manufactured by SLM additive manufacturing. International Journal of Lightweight Materials and Manufacture 2019;2:288–95. https://doi.org/10.1016/j.ijlmm.2019.08.001.

[25] Runyon J, Marsh R, Bowen P, Pugh D, Giles A, Morris S. Lean methane flame stability in a premixed generic swirl burner: Isothermal flow and atmospheric combustion characterization. Exp Therm Fluid Sci 2018;92:125–40. https://doi.org/10.1016/j.expthermflusci.2017.11.019.

[26] Runyon J. Gas Turbine Fuel Flexibility: Pressurized Swirl Flame Stability, Thermoacoustics, And Emissions. Doctor of Philosophy. Cardiff University , 2017.

[27] Stavropoulos P, Foteinopoulos P, Papacharalampopoulos A, Tsoukantas G. Warping in SLM additive manufacturing processes: estimation through thermo-mechanical analysis. The International Journal of Advanced Manufacturing Technology 2019;104:1571–80. https://doi.org/10.1007/s00170-019-04105-2.

[28] Vafadar A, Guzzomi F, Rassau A, Hayward K. Advances in Metal Additive Manufacturing: A Review of Common Processes, Industrial Applications, and Current Challenges. Applied Sciences 2021;11:1213. https://doi.org/10.3390/app11031213.

[29] Ablyaz TR, Shlykov ES, Muratov KR, Sirotenko LD, Matygullina E V. Creation of Textured Surfaces by Electrical Discharge Machining. Russian Engineering Research 2020;40:880–1. https://doi.org/10.3103/S1068798X20100044.

[30] Karmiris-Obratański P, Zagórski K, Papazoglou EL, Markopoulos AP. Surface texture and integrity of electrical discharged machined titanium alloy. The International Journal of Advanced Manufacturing Technology 2021;115:733–47. https://doi.org/10.1007/s00170-020-06159-z.

[31] Obilanade D, Dordlofva C, Törlind P. Surface Roughness Considerations in Design for Additive Manufacturing - A Literature Review. Proceedings of the Design Society 2021;1:2841–50. https://doi.org/10.1017/pds.2021.545.

[32] Subramanian R, Rule D, Nazik O. Dependence of LPBF Surface Roughness on Laser Incidence Angle and Component Build Orientation. Volume 7: Industrial and Cogeneration; Manufacturing Materials and Metallurgy, American Society of Mechanical Engineers; 2021. https://doi.org/10.1115/GT2021-59755.

[33] Koutiri I, Pessard E, Peyre P, Amlou O, De Terris T. Influence of SLM process parameters on the surface finish, porosity rate and fatigue behavior of as-built Inconel 625 parts. J Mater Process Technol 2018;255:536–46. https://doi.org/10.1016/j.jmatprotec.2017.12.043.

[34] Strano G, Hao L, Everson RM, Evans KE. Surface roughness analysis, modelling and prediction in selective laser melting. J Mater Process Technol 2013;213:589–97. https://doi.org/10.1016/j.jmatprotec.2012.11.011.

[35] Mohamed Fahad S, Mahashar Ali J, Siddhi Jailani H. Characterization of Surface Roughness of Ground Specimens Using Image Processing, 2021, p. 133–41. https://doi.org/10.1007/978-981-33-6428-8_9.

[36] Douglas CM, Shaw SL, Martz TD, Steele RC, Noble DR, Emerson BL, et al. Pollutant Emissions Reporting and Performance Considerations for Hydrogen–Hydrocarbon Fuels in Gas Turbines. J Eng Gas Turbine Power 2022;144. https://doi.org/10.1115/1.4054949.

[37] British Standard. ISO 11042-1:1996 Gas Turbines Exhaust Gas Emission Measurement and Evaluation. UK: 1996.

[38] Gaydon AG. The Spectroscopy of Flames. 2nd ed. Netherlands: Springer Netherlands; 1974.

[39] Pugh D, Runyon J, Bowen P, Giles A, Valera-Medina A, Marsh R, et al. An investigation of ammonia primary flame combustor concepts for emissions reduction with OH*, NH2* and NH* chemiluminescence at elevated conditions. Proceedings of the Combustion Institute 2021;38:6451–9. https://doi.org/10.1016/j.proci.2020.06.310.

[40] Pugh D, Valera-Medina A, Bowen P, Giles A, Goktepe B, Runyon J, et al. Emissions Performance of Staged Premixed and Diffusion Combustor Concepts for an NH3/Air Flame With and Without Reactant Humidification. J Eng Gas Turbine Power 2021;143. https://doi.org/10.1115/1.4049451.

[41] British Standard. BS 1134:2010 Assessment of surface texture - Guidance and general information . 2010.

[42] Klingaa CG, Dahmen T, Baier-Stegmaier S, Mohanty S, Hattel JH. Investigation of the roughness variation along the length of LPBF manufactured straight channels. Nondestructive Testing and Evaluation 2020;35:304–14. https://doi.org/10.1080/10589759.2020.1785445.

[43] Lieneke T, Denzer V, Adam GAO, Zimmer D. Dimensional Tolerances for Additive Manufacturing: Experimental Investigation for Fused Deposition Modeling. Procedia CIRP 2016;43:286–91. https://doi.org/10.1016/j.procir.2016.02.361.

[44] Lieneke T, Lammers S, Zimmer D. Geometrical Deviations In Additive Manufacturing-Influences On The Manufacturing Accuracy. Proceedings of the 32nd Annual International Solid Freeform Fabrication Symposium, 2021.

[45] Schlichting H. Boundary Layer Theory. 7th ed. New York : McGraw-Hill; 1979.

[46] Prade B. Gas turbine operation and combustion performance issues. Modern Gas Turbine Systems, Elsevier; 2013, p. 383–423e. https://doi.org/10.1533/9780857096067.3.383.